https://doi.org/10.5194/egusphere-2025-1147
Preprint. Discussion started: 24 March 2025

Continuous chemical characterization of ultrafine particulate matter ($PM_{0.1}$)

Georgia A. Argyropoulou[1,2], Kalliopi Florou[1], and Spyros N. Pandis[1,2]

[1] Institute of Chemical Engineering Sciences, ICE-HT/FORTH, Patras, 265 04, Greece
[2] Department of Chemical Engineering, University of Patras, Patras, 265 04, Greece
Correspondence to: Spyros N. Pandis (spyros@chemeng.upatras.gr)

Abstract. Ultrafine particles (diameter less than 100 nm) are primary suspects for enhanced negative health effects on humans. Measuring the chemical composition and physical properties of ultrafine particles on-line, continuously, and accurately is particularly challenging because of their typically low mass concentration ($PM_{0.1}$) and susceptibility to interference from larger particles. The few past $PM_{0.1}$ chemical composition measurement studies have used cascade impactors and at least daily temporal resolution. In this study we perform for the first time high temporal measurements of the composition and sources of $PM_{0.1}$ using an aerodynamic aerosol classifier (AAC) to separate $PM_{0.1}$ from larger particles. A high-resolution time of flight aerosol mass spectrometer (HR-ToF-AMS, for sulfate, nitrate, organics, chloride), a single particle soot photometer (SP2-XR, for black carbon) and an Xact625i (for elements) are also used.

Ambient $PM_{0.1}$ composition measurements were conducted in a suburban area in Greece to test the system. The hourly $PM_{0.1}$ levels varied from 0.4 to 1.5 μg m^{-3}, with an average of 0.7 μg m^{-3}. Most of the $PM_{0.1}$ (45%) was organic aerosol (OA). On average, sulfates contributed 14%, ammonium 7%, nitrate 3%, and black carbon 4% to $PM_{0.1}$. Calcium (Ca) showed a surprising high average contribution to $PM_{0.1}$ (18%). The rest of the detected elements were Fe, K, Zn and Ti, contributing together 7%. Source apportionment analysis showed that most of the $PM_{0.1}$ OA, during this summertime period, was oxygenated OA (90%), with 70% being less oxidized and 20% being more oxidized, while only 10% was fresh hydrocarbon-like OA.

1. Introduction

Ultrafine particles, also known as UFPs, are particles with diameters less than 0.1 μm and they may represent the most harmful fraction of $PM_{2.5}$ (particulate matter with aerodynamic diameter less than 2.5 μm) (Li et al., 2003; Nel et al., 2006; Schraufnagel, 2020). Exposure to UFPs may lead to increased total and respiratory mortality, respiratory and neurological diseases, and

https://doi.org/10.5194/egusphere-2025-1147
Preprint. Discussion started: 24 March 2025

inflammatory markers (HEI, 2013; Baldauf et al., 2016; Ohlwein et al., 2019). Studies indicate that UFPs are able to translocate to sensitive organs of the human body (e.g., brain) and access systemic circulation (Donaldson et al., 2001; Schraufnagel, 2020).

Several studies have attempted to establish connections between UFP particle number and health outcomes, however reviews by the US EPA (2019) and HEI (2013) have rendered these efforts inconclusive. This difficulty in drawing definitive conclusions may stem from the limited number of studies addressing long-term exposure to UFPs (Ostro et al., 2015; Weichenthal et al., 2017; Ohlwein et al., 2019) or might be associated with the metric used in previous UFP health research (Giechaskiel et al., 2022; Kittelson et al., 2022). The number, surface, and mass concentration of ultrafine particles vary over short spatial and temporal scales as a result of emissions, nucleation, coagulation, condensation, and evaporation (Kumar et al., 2016). While UFPs contribute significantly to particle number concentration, they have relatively low mass concentration (Seinfeld and Pandis, 2016). Their high surface area per unit mass allows them to adsorb greater amounts of toxic substances, a property that renders them primary suspects for enhanced negative health effects on humans (Kumar et al., 2016; Kwon et al., 2020).

The mass concentration of ultrafine particles ($PM_{0.1}$) has been used as health metric by relatively few studies (Kuwayama et al., 2013; Ostro et al., 2015; Yu et al., 2019; Xue et al., 2020a; Xue et al., 2020b). This limited number of studies can largely be attributed to the challenges associated with measuring $PM_{0.1}$ mass, which is more difficult than the measurement of their number concentration (HEI, 2013; Marval and Tronville, 2022). Nonetheless, directing some attention to $PM_{0.1}$ mass concentration is consistent with the gradual shift in focus from TSP (total suspended particles) to PM_{10} (particulate matter of particles with aerodynamic diameter less than 10 μm) to $PM_{2.5}$, to address the increased risks posed by smaller particles (Li et al., 2003; Jalava et al., 2007; Cassee et al., 2019).

The European Union has implemented a particle number regulation for the emissions of solid particles with diameter larger than 23 nm (N_{23}). This selection of solid N_{23} as a regulatory metric was guided mainly by technical concerns rather than the corresponding health effects (Giechaskiel et al., 2021). Low correlation between $PM_{2.5}$ and $PM_{0.1}$ has been frequently recorded (Halek et al., 2010; Eeftens et al., 2015; De Jesus et al., 2019; Mataras et al., 2024), which means that strategies aimed towards reducing $PM_{2.5}$ may not inherently result in reducing $PM_{0.1}$.

https://doi.org/10.5194/egusphere-2025-1147
Preprint. Discussion started: 24 March 2025

UFPs are commonly defined by their number concentrations, although without a standard lower diameter threshold (Kittelson et al., 2022). For $PM_{0.1}$ on the other hand, the challenge lies on the definition of the upper diameter threshold (Kittelson et al., 2022). A definition of $PM_{0.1}$ dependent on the aerodynamic diameter of the particles is consistent with the definitions used for larger particles. However, Tronville et al. (2023) argued that this approach is inappropriate for ultrafine particles, as gravity has a negligible effect on smaller particles, and proposed defining $PM_{0.1}$ based on the physical diameter of particles. In the present study, this definition is adopted and $PM_{0.1}$ represents the mass concentration of particulate matter with physical diameter less than 0.1 μm. For spherical particles, the physical diameter is directly equivalent to their electrical mobility diameter (Hinds, 1999; DeCarlo et al. 2004).

Newly formed particles are introduced into the atmosphere through either primary sources or secondary formation (Seinfeld and Pandis, 2016; Kumar et al., 2016; Abdillah and Wang, 2023). In urban atmosphere typical combustion sources are traffic, domestic biomass burning, residential or commercial cooking, etc. Burning of agricultural waste, forest fires, power plants and other industrial sources are important in regional scales (Kumar et al., 2016; Moreno-Rio et al., 2021). Secondary particles are the product of the atmospheric chemical conversion of gas-phase pollutants (SO_2, NH_3, volatile and intermediate-volatility organic compounds) to low-volatility products (H_2SO_4, HNO_3, low volatility organics, and ammonium salts), which are then transferred to the particulate phase through either nucleation or condensation (Seinfeld and Pandis, 2016).

The sources of ultrafine particle number and mass tend to be significantly different (Yu et al., 2019). UFP number concentration is mainly influenced by nucleation events, which typically occur during high photochemically active periods, when particulate matter concentrations are quite low, and vapors are unable to condense rapidly on pre-existing particles (Zhang et al., 2015; Giechaskiel et al., 2022). In contrast, nucleation is a minor, or even negligible, source for $PM_{0.1}$ mass concentration (Zhang et al., 2015; Yu et al., 2019). The main contributors to ultrafine particle mass are the condensation of secondary organic particulate matter and sulfate (Xue et al., 2020a; Xue et al., 2020b).

Measuring the chemical composition and physical properties of ultrafine particles continuously and accurately is particularly challenging because of their typically low mass concentrations and the potential for interference from larger particles during measurement. The few past $PM_{0.1}$ chemical composition studies have used some type of cascade impactor

https://doi.org/10.5194/egusphere-2025-1147
Preprint. Discussion started: 24 March 2025

(Kuwayama et al., 2013; Ostro et al., 2015; Corsini et al., 2017; Marcias et al., 2018; Yu et al., 2019; Xue et al., 2020a; Xue et al., 2020b; Beauchemin et al., 2021; Phairuang et al., 2022). However, this approach for $PM_{0.1}$ measurement provides low temporal resolution (daily or longer intervals), requires substantial labor, and may yield results influenced by the presence of larger particles that have substantially higher mass.

In this study, we propose an approach for the continuous, automatic measurement of $PM_{0.1}$ chemical composition, using the aerodynamic aerosol classifier (AAC, Cambustion) adjusted to operate as a low-pass separator, to separate $PM_{0.1}$ from larger particles, followed by instruments that provide continuous chemical composition measurements and/ or mass spectra. The AAC was also coupled with a Scanning Mobility Particle Sizer (SMPS) to provide information about effective density. The system is tested in a pilot field study to obtain insights into the continuous chemical characterization, physical properties and source apportionment of $PM_{0.1}$.

2. Experimental approach

2.1 The AAC as a $PM_{0.1}$ separator

The aerodynamic aerosol classifier (AAC, Cambustion) is designed to transmit practically monodisperse particles of a selected aerodynamic diameter from 25 nm to over 5 μm. This is achieved by directing the inlet polydisperse aerosol though a rotating cylinder, in which particles are subjected to opposing centrifugal and drag forces. The particles of the selected size follow the intended trajectory and exit through the sample outlet (monodisperse flow) (Fig. 1).

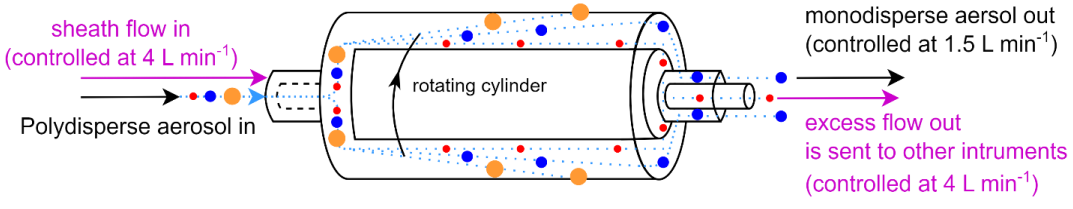

Figure 1. Principle of Operation of the AAC when adjusted as a separator.

Particles that are larger than the specified size impact the outer wall of the classifier, while particles that are smaller than the specified size exit through the sheath outlet (excess flow). During normal

https://doi.org/10.5194/egusphere-2025-1147
Preprint. Discussion started: 24 March 2025

operation, this excess flow, containing the unwanted particles that are smaller than the specified size, is internally filtered and recirculated as sheath flow back into the AAC (Tavakoli and Olfert, 2013).

The AAC flow system can be adjusted so that the excess flow containing these 'unwanted particles' can be utilized. Instead of recirculating this excess flow back into the AAC, it can be discharged outside the instrument and redirected to other systems (Fig. 1). This modification dilutes the outlet flows (monodisperse flow and excess flow) by a factor equal to the selected (sheath flow in) / (polydisperse flow in) ratio, as the AAC continues to draw filtered clean air through the sheath flow inlet. To ensure proper functionality, the outlet flows must be externally controlled using mass flow controllers (MFC), as this adjustment deviates from the standard operation of the instrument. Accurate size classification and dilution require that the sheath flow in matches the excess flow out, necessitating continuous monitoring of the sheath flow, monodisperse flow, and excess flow. Under these conditions, the AAC operates effectively as a selectable cut-off size separator. In this study, the sheath flow in and the excess flow out were controlled at 4 L min^{-1}, while the polydisperse flow in and monodisperse flow out were maintained at 1.5 L min^{-1}. This configuration optimized the cut-off sharpness and minimized the dilution, resulting in a dilution factor of approximately 2.7.

The system was tested using ambient laboratory air to ensure that the dilution and the sharpness of the cut-off are suitable for the typically low $PM_{0.1}$ concentrations, and that there are no significant $PM_{0.1}$ losses within the AAC. The monodisperse flow rate was controlled at 1.5 L min^{-1} with a mass flow controller (MFC; Bronkhorst EL-FLOW Prestige Mass Flow Meter/ Controller) before being directed to an exhaust pump (Fig. S1). The excess flow rate was maintained at 4 L min^{-1}. A part of these 4 L min^{-1} equal to 0.6 L min^{-1} was sampled by an SMPS (TSI Classifier model 3080, DMA model 3081, CPC 3775), while the remaining 3.4 L min^{-1} was exhausted through an MFC. A bypass line connected the SMPS to the front of the AAC, allowing the SMPS to alternate sampling between the bypass line and the excess flow line every 30 min over a 2-hour period. The relatively long alternation interval was chosen to verify that the system required minimal time to stabilize the externally controlled flows and achieve a sharp and stable cut-off. Since ambient laboratory air exhibited stable particle concentrations and size distributions, this interval did not affect the accuracy of the results.

https://doi.org/10.5194/egusphere-2025-1147
Preprint. Discussion started: 24 March 2025

The mass penetration of $PM_{0.1}$ was calculated by comparing the average mass size distributions measured by the SMPS between the bypass line and excess flow (Fig. S2). The AAC cut-off (cut diameter where there is 50% mass penetration, d_{50}) was set to an aerodynamic diameter of 140 nm, corresponding to an electrical mobility diameter of 100 nm. For spherical particles, the electrical mobility diameter is equivalent to their physical diameter (Hinds, 1999; DeCarlo et al., 2004). Since $PM_{0.1}$ is defined, in this study, based on the physical particle diameter, the system was calibrated using the electrical mobility diameter as a proxy for the physical diameter d_{50} to be at 100 nm. The mass penetration at the target d_{50} of 100 nm was approximately 50%, while for particles smaller than 100 nm, it reached 90%. For larger particles, the mass penetration was less than 10% at 120 nm, decreasing to below 5% at 200 nm, and near zero for particles larger than 300 nm. These results demonstrate that the AAC can effectively function as a $PM_{0.1}$ separator at ambient concentrations, with minimal particle losses.

A second test was conducted to determine the $PM_{0.1}$ losses when the AAC outlet flows (monodisperse flow and excess flow) pass through an MFC. This evaluation was necessary because, in the main experimental setup, a portion of the excess flow must pass through an MFC, to ensure that the excess flow rate is maintained at the desired value of 4 L min^{-1}, before being directed to a chemical composition measurement instrument.

In this test, the AAC was continuously supplied with polydisperse ammonium sulfate particles at various concentrations. An ammonium sulfate solution of 5 g L^{-1} was atomized using a constant output atomizer (TSI 3076). Part of the atomized ammonium sulfate passed through a HEPA filter and part went directly to the AAC to control the measured concentrations (Fig. S3). The monodisperse flow and the excess flow rates were controlled with separate MFCs at 1.5 L min^{-1} and 4 L min^{-1}, respectively, having a combined flow equal to 5.5 L min^{-1}. The ammonium sulfate aerosol passing though the MFCs was sampled by an SMPS (TSI 3034) sampling at 1 L min^{-1} and the remaining 4.5 L min^{-1} was exhausted with the help of a pump. As in the previous test, a bypass line connected the SMPS to the front of the AAC and the SMPS sampling alternated between the bypass line and the outlet flows of the AAC every 30 min over a 2-hour period. The concentrations sent to the system were stable, so the long time-interval did not affect the accuracy of the results.

The AAC cut-off was again set to an aerodynamic diameter of 140 nm, corresponding to a d_{50} electrical mobility diameter of 100 nm (Fig. S4). Mass penetration was calculated, as before,

https://doi.org/10.5194/egusphere-2025-1147
Preprint. Discussion started: 24 March 2025

by comparing the average mass size distributions measured by the SMPS between the bypass line and the outlet flows line. At the 100 nm electrical mobility diameter cut-off, the mass penetration was 50%, while for particles between 50-100 nm it was over 80% (Fig. S4). These results confirm that the system exhibits minimal losses, even when aerosol flows pass through MFCs for $PM_{0.1}$.

2.2 The continuous $PM_{0.1}$ chemical characterization system

A schematic of the experimental set-up is shown in Fig. 2. The ambient inlet air first passed through a $PM_{2.5}$ Sharp Cut Cyclone (SCC; AAVOS International) at 16.7 L min^{-1}, to extend the interval between required cleanings of the AAC's outer cylinder, where larger particles impact.

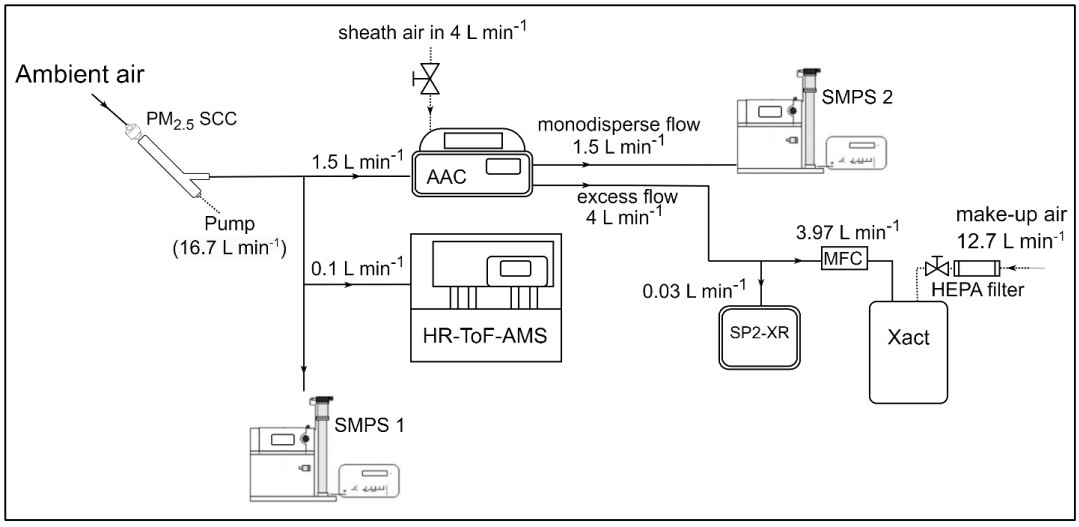

Figure 2. Experimental set-up for the continuous $PM_{0.1}$ chemical characterization system.

The ambient aerosol size distribution was measured by an SMPS (SMPS-1; TSI Classifier model 3080, DMA model 3081, CPC 3775), and its size/ composition distribution by a High-Resolution Time-of-Flight Aerosol Mass Spectrometer (HR-ToF-AMS; Aerodyne Research Inc.; DeCarlo et al., 2006). The SMPS-1 continuously measured the total $PM_{0.1}$ and provided size distributions for electrical mobility diameters from 10 nm to 505 nm, with a sample flow of 1 L min^{-1} and a sheath flow of 5 L min^{-1}. The HR-ToF-AMS measured the size-resolved chemical composition of sub-micrometer aerosols (specifically organics, nitrate, sulfate, chloride, and

https://doi.org/10.5194/egusphere-2025-1147
Preprint. Discussion started: 24 March 2025

ammonium). The vaporizer surface temperature was 600°C. The HR–ToF–AMS data was gathered at three-minute intervals with sampling flow at approximately 0.1 L min^{-1}.

The AAC was operating as a $PM_{0.1}$ separator, with the d_{50} cut diameter set at 140 nm aerodynamic diameter (100 nm electrical mobility diameter, and physical diameter for spherical particles). The AAC was set to operate with a polydisperse inlet flow equal to 1.5 L min^{-1}, and provided two outlet flows: (1) the monodisperse outlet flow, which was controlled at 1.5 L min^{-1}, and directly sent to a second SMPS (SMPS 2; TSI Classifier model 3080, DMA model 3081, CPC 3787), and (2) the excess outlet flow, which contained the smaller than the selected cut-off particles and was controlled at 4 L min^{-1}. This excess outlet flow was analyzed using two instruments. A single particle soot photometer (SP2-XR; Droplet Measurement Technologies), measured refractory black carbon (rBC) continuously, and had a sample flow of 0.03 L min^{-1} and a sheath flow of 0.06 L min^{-1}. An Xact 625i (SailBri Cooper Inc.), measured concentration of elements semi-continuously (4-hour sampling).

The Xact samples with a 16.7 L min^{-1} flow. To ensure that the excess outlet flow from the AAC remained at 4 L min^{-1}, the aerosol sampled by the Xact passed through an MFC set at 3.97 L min^{-1}. This value was calculated by subtracting the SP2-XR sampling rate of 0.03 L min^{-1} from the desired total of 4 L min^{-1}. The remaining 12.73 L min^{-1} of the Xact sample flow was provided as clean air, which diluted the samples measured by the Xact by approximately 11.

Ambient $PM_{0.1}$ chemical composition measurements were performed in Patras (38° 17' N 21° 48' E), Greece, at the Institute of Chemical Engineering Sciences (ICE-HT/ FORTH) between 17-29 July 2024. The station is located in a suburban area approximately 9 km northeast of the city center. During summer in southern Greece, ambient temperatures are typically high, and relative humidity is below 40% (Fig. S5), so the inlet air was not dried for these measurements. All sampling lines used in this study were stainless steel to avoid potential artifacts from conductive silicone tubing (Timko et al., 2009).

For a three-day period (July 29 to 1 August) the HR-ToF-AMS was set up to collect spectra attributed specifically to $PM_{0.1}$ by positioning it downstream of the AAC, configured to function as a $PM_{0.1}$ separator, again with a d_{50} set at 140 nm aerodynamic diameter, and with the same flow settings as in the previous experimental set-up (Fig. 3). The monodisperse outlet flow was controlled with an MFC at 1.5 L min^{-1} and in this case exhausted through a pump. The excess outlet flow containing the particles smaller than the selected cut-off was sampled by the HR-ToF-

https://doi.org/10.5194/egusphere-2025-1147
Preprint. Discussion started: 24 March 2025

AMS and by an SMPS (TSI Classifier model 3080, DMA model 3081, CPC 3775). The SMPS had a sample flow equal to 0.6 L min^{-1} and was used to calculate the AMS collection efficiency. The remaining 3.3 L min^{-1}, out of the total 4 L min^{-1} that was the controlled flow rate of the excess flow, was exhausted through a pump.

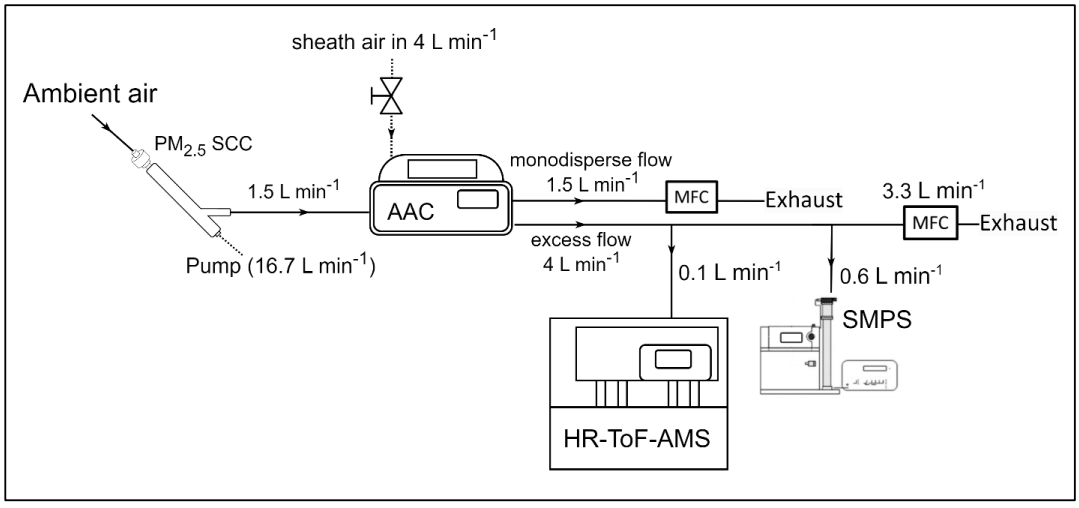

Figure 3. Experimental set-up for the continuous source apportionment of $PM_{0.1}$ organic aerosol (OA).

3. Data analysis

3.1 HR-ToF-AMS data analysis

The AMS data was processed using the standard SQUIRREL software (v1.66E) within Igor Pro (Wavemetrics), along with the PIKA package (v1.26E) for high-resolution peak integration. Elemental ratios measured by the HR-ToF-AMS were determined using the improved ambient calculation method proposed by Canagaratna et al. (2015). The collection efficiency (CE) for the HR-ToF-AMS was assessed by combining HR-ToF-AMS mass distributions (vacuum aerodynamic diameters approximately from 40 to 150 nm) with the SMPS-1 volume distributions (electrical mobility diameters from 10 to 100 nm) and applying the Kostenidou et al. (2007) algorithm every two hours. The same algorithm was used to determine the PM_1 organic aerosol (OA) density. The upper limit of the HR-ToF-AMS mass distributions, approximately 150 nm vacuum aerodynamic diameter, was selected based on the particle density of the measured aerosol.

https://doi.org/10.5194/egusphere-2025-1147
Preprint. Discussion started: 24 March 2025

For a particle density of 1.5 g cm^{-3} and spherical particles, this corresponds to a physical diameter of about 100 nm (DeCarlo et al., 2004), consistent with the $PM_{0.1}$ definition used in this study. AMS data between 17-29 July 2024 were then averaged over 4-hour intervals to align with the Xact dataset, with negative values replaced with zero values.

3.2 Xact625i data analysis

The 4-hour Xact samples were corrected for both positive artifacts and dilution effects. The Xact uses reel-to-reel Teflon filter tape sampling and nondestructive energy dispersive X-ray fluorescence (EDXRF) analysis (Tremper et al., 2018, Furger et al., 2017). While this analytical method is highly effective even for low concentrations, it is susceptible to positive artifacts. To address positive artifacts in the Xact samples and to determine the limit of detection (LOD) for each element, blank measurements were conducted. For these blank measurements, a HEPA filter was placed upstream of the $PM_{2.5}$ cyclone to assess potential artifacts introduced by components situated between the ambient air inlet and the Xact (Fig. 2). These components included the tubing, the $PM_{2.5}$ cyclone, the AAC, and one MFC. The LOD for each element *i* was calculated following the IUPAC Recommendations (Currie, 1995) and the JRC Publications Resitory using the equation:

$$\mathrm{LOD}_i = \mu_{\mathrm{blank},i} + k_\alpha \sigma_{0,i} + k_\beta \sigma_{0,i}, \quad (1)$$

where $\mu_{\mathrm{blank},i}$ represents the mean value of the blank measurements for element *i*, and $\sigma_{0,i}$ is the standard deviation of the blank measurements for the same element. The terms k_α and k_β are numerical factors associated with the α-error and β-error, respectively. The α-error corresponds to the risk of falsely detecting the analyte when it is not present, while the β-error corresponds to the risk of failing to detect the analyte when it is present. These factors are chosen based on the desired confidence level. For a 90% confidence level for both α-error and β-error, and 3 degrees of freedom (calculated as the number of our blank samples minus 1), k_α and k_β are equal to one-tailed Student's *t* value. In this case, $k_\alpha = k_\beta = 1.64$. Substituting these values into Eq. (1) simplifies to:

$$\mathrm{LOD}_i = \mu_{\mathrm{blank},i} + 3.3\,\sigma_{0,i}, \quad (2)$$

https://doi.org/10.5194/egusphere-2025-1147
Preprint. Discussion started: 24 March 2025

The dilution factor for the Xact samples (DF_{Xact}) was calculated based on the total air volume that was measured by the Xact for each sample (V_{Xact}), which can be slightly different from sample to sample, depending on ambient temperature. So, the DF_{Xact} combining also the dilution factor by the AAC (DF_{AAC}) working as a $PM_{0.1}$ separator was calculated as:

$$DF_{Xact} = \frac{V_{Xact}}{3.97\ t}\ DF_{AAC}, \quad (3)$$

where t is the sampling time in minutes, and 3.97 L min^{-1} represents the flow rate into the Xact after the AAC-$PM_{0.1}$-separator (Fig. 2). The sampling time for the 4-hour samples was 240 min. The Xact performs an automated quality assurance test every midnight, which reduces the sampling time of the midnight samples by approximately 30 min. The DF_{Xact} values varied from 9.7 (for the midnight samples) to 11.15. Each Xact sample was corrected based on its specific DF_{Xact}.

The Xact detected the elements Si, S, Cl, K, Ca, Ti, Fe and Zn (Fig. S6). During the summer months in Patras, $PM_{0.1}$ concentrations are typically low (Argyropoulou et al., 2024), resulting in measured element concentrations that were close to their respective limits of detection (LODs). When measured concentrations are close to the LODs the lighter elements Si, S, Cl, K, Ca are more susceptible to self-absorption effects, which increase the uncertainty of their measurements (Furger et al., 2017). Although this uncertainty is generally independent of the Xact's tube temperature, Si exhibited a moderate to high correlation (R^2 = 64%) with the tube temperature of the instrument (Fig. S7). Due to this potential temperature-related artifact, Si was excluded from the main results. The levels of the rest of the detected elements had low to no correlation with the tube temperature of the instrument.

The Xact 4-hour samples that were below their respective LODs were replaced with zero values. The elements S, Cl, K, Ca, Ti, Fe and Zn were corrected by subtracting their respective blank value and then multiplying the non-negative values by the respective sample-dilution-factor (Eq. (3)) (Fig. S8).

The corrected average values of S and Cl from the Xact were compared with the average sulfate and chloride concentrations measured by the AMS. During the measurement period from 17 to 29 July 2024, the average S concentration from the Xact (multiplied by 3 to match the sulfate

https://doi.org/10.5194/egusphere-2025-1147
Preprint. Discussion started: 24 March 2025

concentrations by the AMS) was on average 96.2 ng m^{-3}, closely aligning with the AMS-measured sulfate concentration of 100.7 ng m^{-3}. The average Cl concentration from the Xact was 7.2 ng m^{-3}, compared to 13.5 ng m^{-3} for chloride from the AMS. However, the correlation between Xact and AMS measurements over shorter time intervals was low. This can be attributed to measured values being near their respective limits of detection (LODs) and uncertainties associated with the measurement of light elements. Moreover, the low number of measured samples means that even a few mismatched data points can significantly reduce the correlation between datasets. Thus, for the main results, the timeseries of sulfate and chloride concentrations measured by the AMS are shown, rather than the S and Cl measurements from the Xact. For the remaining measured elements and the complete $PM_{0.1}$ composition, only average values over the entire measurement period (17–29 July 2024) are shown, as Xact measurements for shorter time intervals were deemed rather uncertain for these low $PM_{0.1}$ concentrations of the sampling location.

4. Ambient $PM_{0.1}$ chemical composition

The $PM_{0.1}$ estimated from the SMPS-1 measurements for an effective density equal to 1.5 g cm^{-3}, had an average concentration of 0.69 ± 0.28 µg m^{-3}, ranging from minimum 0.4 µg m^{-3} to maximum 1.5 µg m^{-3} (15 min averages) (Fig. 4). $PM_{0.1}$ peaked in the morning, between 6:00 and 8:00 local time (LT), primarily due to increased rBC concentrations associated with morning traffic (Fig. 5). Concentrations of all $PM_{0.1}$ species began to increase during the evening from 20:00 LT to midnight.

The average refractory $PM_{0.1}$ BC concentration was 0.038 ± 0.074 µg m^{-3}, with values ranging from minimum 0.003 to maximum 0.059 µg m^{-3} (15 min averages) (Fig. 4). $PM_{0.1}$ rBC peaked during early morning hours (07:00 LT) and had a smaller peak in the evening (20:00–24:00 LT) (Fig. 5). On average, rBC contributed 4.0% to total $PM_{0.1}$, with contributions ranging from 1% to 19% at hourly scales (Fig. 6).

https://doi.org/10.5194/egusphere-2025-1147
Preprint. Discussion started: 24 March 2025

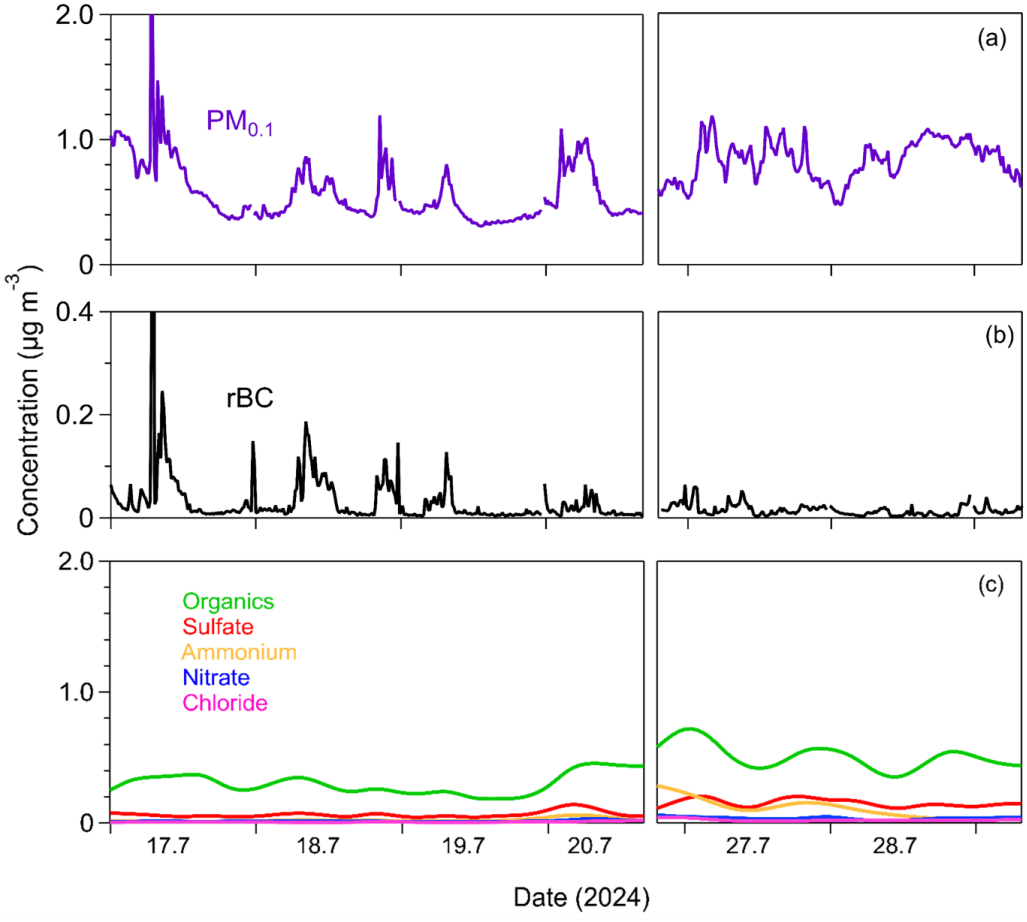

Figure 4. Timeseries of (a) particle mass concentration of particles with diameters below 0.1 µm ($PM_{0.1}$) measured by SMPS-1, (b) $PM_{0.1}$ refractory black carbon (rBC) measured by the SP2-XR (c) $PM_{0.1}$ organics, sulfate, ammonium, and nitrate measured by the HR-ToF-AMS, in Patras, Greece, from 17 to 29 July 2024. The time resolution for $PM_{0.1}$ and rBC is 15 min, while for organics, sulfate, ammonium, and nitrate the time resolution is 4 hours.

The organic $PM_{0.1}$ mass concentration had an average value of 0.34 ± 0.17 µg m^{-3} (Fig.4), making it the largest contributor to total $PM_{0.1}$ (45%) (ranging from 23% to 71%). The $PM_{0.1}$ OA concentrations remained relatively stable, with minor peaks at night (22:00 LT) and early in the morning (06:00 LT) (Fig. 5).

https://doi.org/10.5194/egusphere-2025-1147
Preprint. Discussion started: 24 March 2025

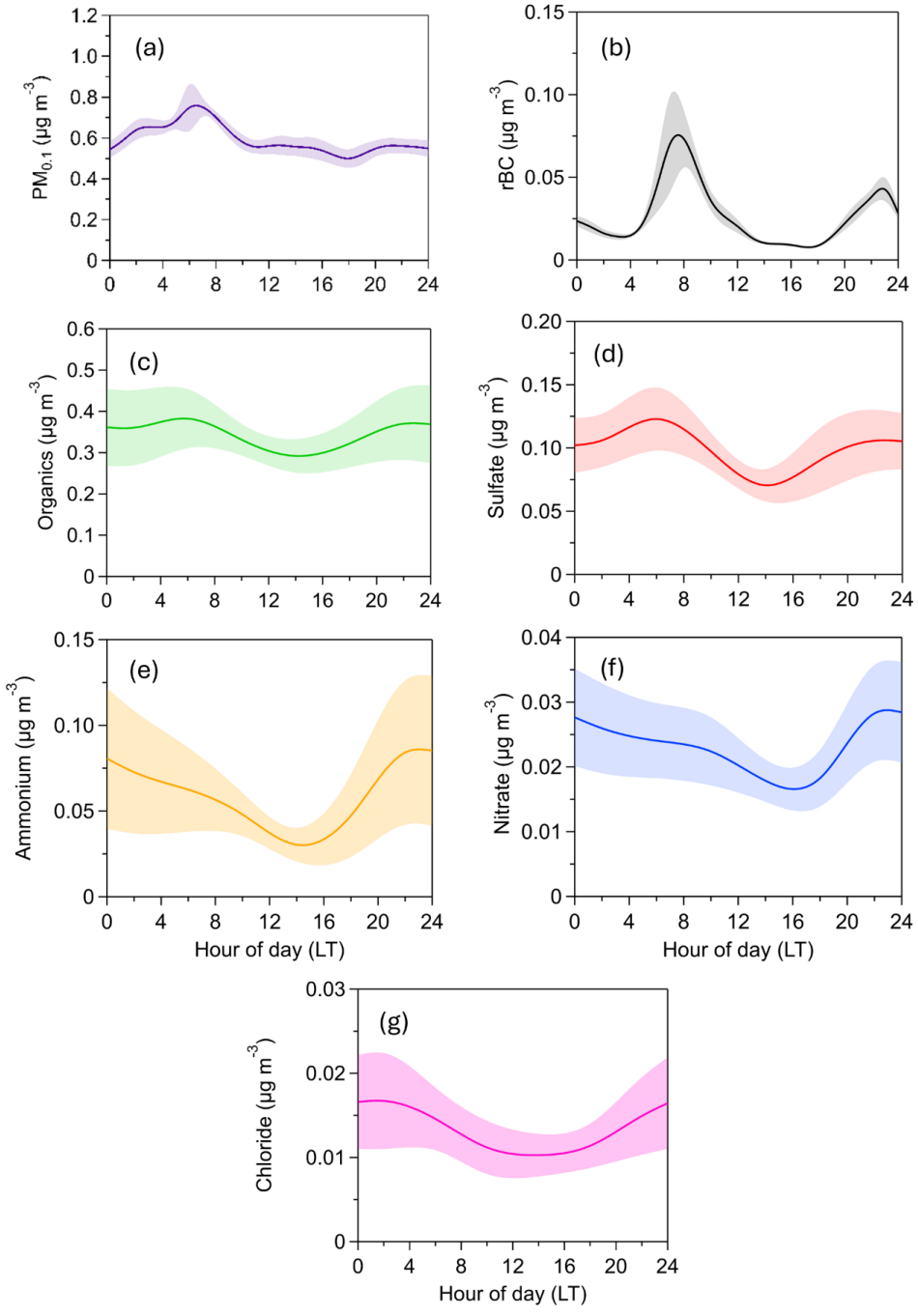

Figure 5. Diurnal variation of $PM_{0.1}$ concentration and composition. The shaded areas correspond to the standard deviation of the mean.

https://doi.org/10.5194/egusphere-2025-1147
Preprint. Discussion started: 24 March 2025

Sulfate had an average concentration of 0.10 ± 0.05 μg m^{-3} (Fig. 4), and contributed 14% to $PM_{0.1}$ on average (Fig. 6), with contributions ranging from 6% to 25%. Sulfate concentrations peaked early in the morning (06:00 LT) and showed a secondary, less pronounced increase at night (22:00 LT).

Ammonium had an average concentration of 0.06 ± 0.07 μg m^{-3}, while nitrate averaged 0.02 ± 0.01 μg m^{-3} (Fig. 4). Their contributions to $PM_{0.1}$ were 7% (ranging from 1% to 19%) and 3.0% (ranging from 1% to 6%), respectively (Fig. 6). Both ammonium and nitrate concentrations peaked at night (22:00 LT) and decreased to their minimum levels midday (14:00 LT) (Fig. 5).

Chloride had an average concentration of 0.013 ± 0.010 μg m^{-3} (Fig. 4). Its concentration was relatively stable, with a slight increase late at night (02:00 LT) (Fig. 5). Chloride contributed an average of 1.7% to $PM_{0.1}$, with contributions ranging from 0.4% to 4% (Fig.6).

The corrected mean concentrations of elements in $PM_{0.1}$ measured by the Xact followed the order: Ca > Fe > K > Zn > Ti (Fig. S8). The average mass concentrations were 130.5 ng m^{-3} for Ca, 29.6 ng m^{-3} for Fe, 19.6 ng m^{-3} for K, 1.4 ng m^{-3} for Zn, and 1.1 ng m^{-3} for Ti. Their respective contributions to $PM_{0.1}$ were 18.2% for Ca, 4.3% for Fe, 2.8% for K, 0.2% for Zn, and 0.2% for Ti (Fig. 6).

The daily averages of the summed concentrations of all measured species (organics, sulfate, ammonium, nitrate, chloride, rBC, Ca, Fe, K, Zn and Ti) were compared to the daily average $PM_{0.1}$ concentrations estimated from SMPS-1 measurements, for effective density of 1.5 g cm^{-3} (Fig. 6). This comparison was performed to assess their agreement and evaluate the closure of the chemical balance of $PM_{0.1}$. The best-fit regression line had a slope of 0.75 and an intercept of 0.21 μg m^{-3}, with an R^2 value of 42%. When constrained to pass through zero, the regression line had a slope of 1.03. Most of the daily averages fell within the ±20% deviation lines, with the remainder within ±40%.

5. Effective density estimation of $PM_{0.1}$

The effective density (ρ_{eff}) of $PM_{0.1}$ was estimated in this study using two approaches. The first approach was by estimating ρ_{eff} from the measured chemical composition of $PM_{0.1}$. For this approach, the OA hourly effective density was calculated by the Kostenidou et al. (2007) algorithm. A density of 1.8 g cm^{-3} was assumed for BC (Taylor et al., 2015). The effective density of $PM_{0.1}$ derived from the chemical composition measurements was 1.47 ± 0.02 g cm^{-3} (Fig. 7).

https://doi.org/10.5194/egusphere-2025-1147
Preprint. Discussion started: 24 March 2025

The second approach for the $PM_{0.1}$ ρ_{eff} estimation was by continuously directing the monodisperse ambient aerosol from the AAC (set at 140 nm aerodynamic diameter) to the SMPS-2 (AAC/SMPS in tandem) (Fig. 2). This setup produced a monodisperse aerosol distribution with an electrical mobility diameter of approximately 100 nm (Fig. S9). For spherical particles, this electrical mobility diameter is equivalent to the physical diameter (DeCarlo et al., 2004; Hinds, 1999). This estimation method relies solely on the monodisperse distribution of 100 nm particles and provides a rapid and straightforward means to approximate ρ_{eff} for $PM_{0.1}$. Given that the majority of $PM_{0.1}$ lies near 100 nm, deriving the effective density in this range offers a reasonable estimate of the ρ_{eff} for $PM_{0.1}$.

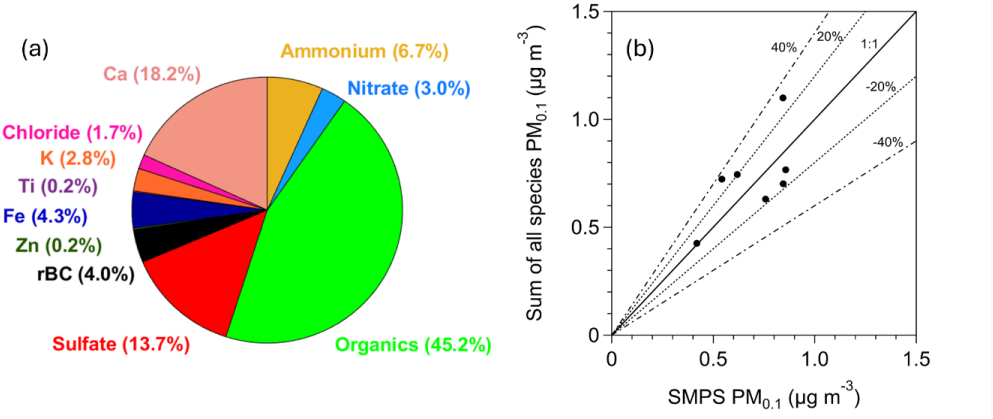

Figure 6. (a) Average $PM_{0.1}$ chemical composition for the period of measurements (17 to 29 July 2024) in Patras, Greece. (b) Daily average of the sum of the measured $PM_{0.1}$ species versus daily average of the $PM_{0.1}$ measured by the SMPS, for effective density equal to 1.5 g cm^{-3}. The black line corresponds to the 1:1 line, and the dashed lines correspond to the ± 20% and ± 40%, respectively.

The particle's electrical mobility (B) is calculated using the electrical mobility diameter (d_{mo}) measured by the SMPS-2:

$$B = \frac{C_c(d_{mo})}{3\pi\mu d_{mo}}, \quad (4)$$

https://doi.org/10.5194/egusphere-2025-1147
Preprint. Discussion started: 24 March 2025

where μ represents the viscosity of the carrier gas, and C_c is the Cunningham slip correction factor for the corresponding d_{mo} (Kim et al., 2005). The hourly average of the peak of the monodisperse distribution measured by the SMPS-2 was used for d_{mo} (Fig. S9).

The particle's mass (m) is then calculated using the derived B and the aerodynamic diameter (d_{ae} = 140 nm) set on the AAC:

$$m = \frac{C_c(d_{ae})\rho_0 d_{ae}^2}{18\mu B}, \quad (5)$$

where C_c is the Cunningham slip correction factor of the corresponding d_{ae} (Kim et al., 2005), and ρ_0 is the reference density equal to 1000 kg m^{-3}. Finally, the ρ_{eff} can be expressed as:

$$\rho_{eff} = \frac{m}{(\pi/6)\, d_{mo}^3}, \quad (6)$$

Substituting m from Eq. (5) into Eq. (6) allows the calculation of ρ_{eff}.

The effective density derived from the AAC/SMPS in tandem approach was on average 1.51 ± 0.04 g cm^{-3}, consistent with the $PM_{0.1}$ ρ_{eff} that was determined through chemical composition measurements (Fig. 7). The average effective density over the measurement period derived from both approaches (estimation by chemical composition, and estimation by AAC/SMPS in tandem) was equal to 1.5 g cm^{-3}. This value has been consistently applied throughout this study.

6. Sources of $PM_{0.1}$ organic aerosol

To identify the various sources of OA, Positive Matrix Factorization (PMF) analysis was conducted, using high-resolution AMS organic mass spectra (m/z values from 12 to 120) as input data (Lanz et al., 2007; Paatero and Tapper, 1994; Ulbrich et al., 2009) for a three-day period (July 29 to 1 August). The PMF analysis, applied to a high-temporal-resolution dataset of approximately 700 data points (3-minute intervals), yields reasonable results.

Analysis was performed using both the unconstrained PMF method (Ulbrich et al., 2009) and the Multilinear Engine algorithm (ME-2; Paatero, 1999), with the latter at varied α values

https://doi.org/10.5194/egusphere-2025-1147
Preprint. Discussion started: 24 March 2025

using the Source Finder (SoFi) software (Canonaco et al., 2013). The factors in both methods varied from one to seven, and different f_{peak} values were tested, ranging from −1 to 1 in 0.2 increments. ME-2 is helpful when PMF results are inconclusive or when smaller source contributions need better quantification. The primary difference between PMF and ME-2 is that ME-2 allows users to input prior information on factor profiles, forcing the algorithm to account for specific sources.

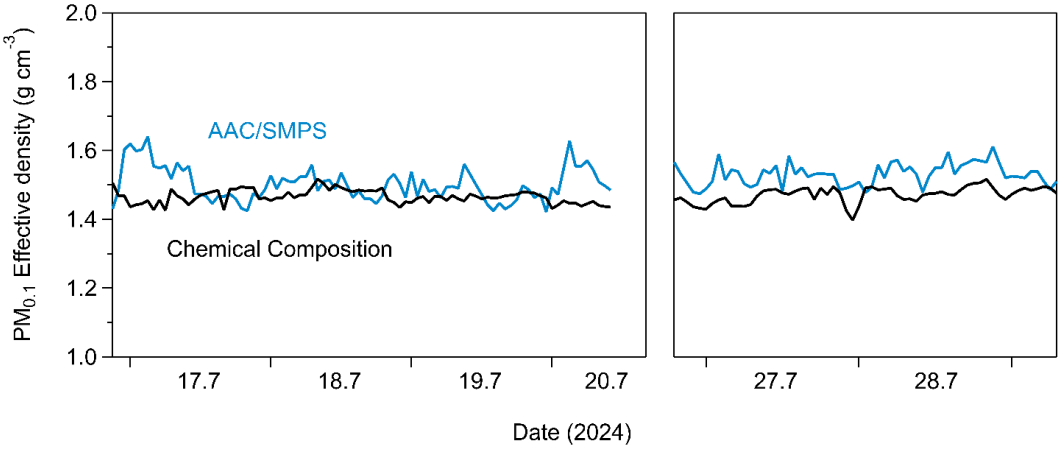

Figure 7. Hourly effective density of $PM_{0.1}$ estimated by the chemical composition measurements (black line) and by combining the AAC with an SMPS (blue line) (Tavakoli and Olfert, 2014).

A two-factor solution in PMF was initially explored to assess the composition of $PM_{0.1}$ OA. This analysis identified two distinct secondary organic aerosols (SOA) factors: a more-oxidized oxygenated organic aerosol (MO-OOA) factor and a less-oxidized oxygenated organic aerosol (LO-OOA) factor. The MO-OOA accounted for 58% of the $PM_{0.1}$ OA mass, with an O:C ratio of 0.8, indicating a higher degree of oxidation. In contrast, the LO-OOA contributed 42% of the $PM_{0.1}$ OA mass and exhibited a lower O:C ratio of 0.6. Notably, the high-resolution (HR) spectra of the two factors were highly similar (R^2=0.96), and their time series showed strong anticorrelation (Fig. S10). These findings suggested that a two-factor solution might oversimplify the data and that a more nuanced representation could be achieved by increasing the number of factors.

https://doi.org/10.5194/egusphere-2025-1147
Preprint. Discussion started: 24 March 2025

To better characterize the sources of $PM_{0.1}$ OA, a three-factor solution was subsequently adopted in the PMF analysis. This approach resolved three oxygenated organic aerosol (OOA) factors: a more-oxidized OOA (MO-OOA) factor, a less-oxidized OOA (LO-OOA) factor, and an oxidized primary OA (OPOA) factor (Fig. 8). The average O:C ratio during this period was 0.64 ± 0.04, implying that indeed the $PM_{0.1}$ aerosol was rather aged. The HR spectra for the three resolved OA factors are presented in Fig. S11.

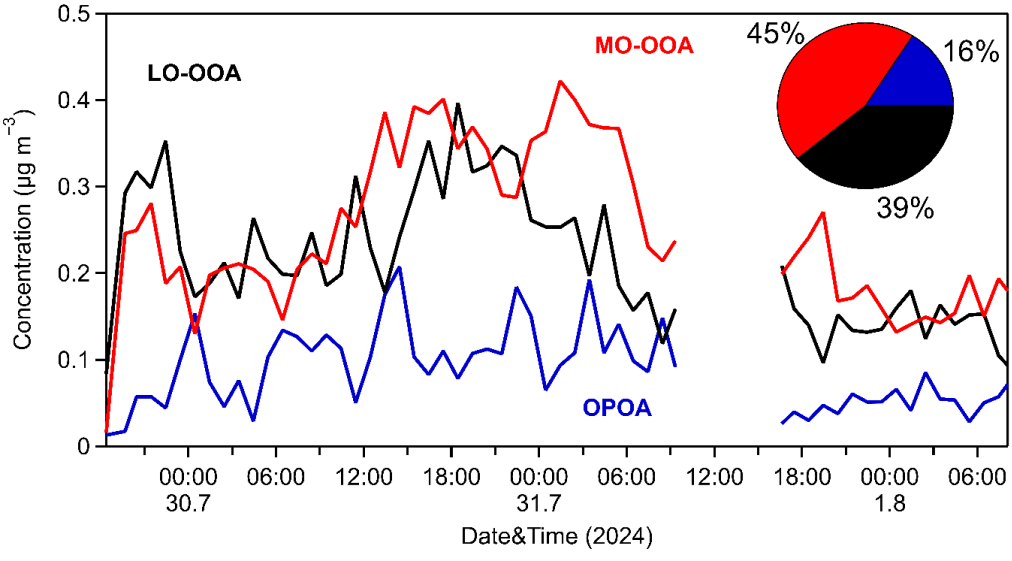

Figure 8. Hourly time-series of the PMF factors for $PM_{0.1}$ OA.

The MO-OOA factor dominated during the 3-day measurement period, representing around 45% of the $PM_{0.1}$ OA with an average concentration of 0.25 μg m^{-3}, while its hourly maximum value was equal to 0.4 μg m^{-3}. Its O:C was 0.96 and its correlation to $PM_{0.1}$ sulfate and nitrate was medium (R^2 = 0.43 and 0.48, respectively). The LO-OOA contributed 39% to OA with a mean value of 0.2 μg m^{-3}. Its O:C was equal to 0.6 and correlated reasonably well with particulate $PM_{0.1}$ sulfate (R^2 =0.60) (Fig. S12). Both MO-OOA and LO-OOA factors were dominated by $C_xH_yO^+$ and $C_xH_yO_z^+$ families (62% and 50%, respectively), while the $C_xH_y^+$ family was responsible for 21% (MO-OOA) and 36% (LO-OOA) of each spectrum. An OPOA factor was identified as the third factor during the measurements, characterized by intermediate O:C of 0.42,

https://doi.org/10.5194/egusphere-2025-1147
Preprint. Discussion started: 24 March 2025

indicative of moderate chemical aging occurring during or shortly after emission. It represented 16% of the $PM_{0.1}$ OA. Its mass spectrum exhibited features that distinguish it from both POA and secondary organic aerosols (SOA) and features prominent peaks at *m/z* 28 (CO^+), 43 ($C_2H_3O^+$), and 44 (CO_2^+), reflecting the presence of oxygen-containing functional groups. While its spectrum retains characteristic peaks of primary organic aerosols (POA) such as hydrocarbon-like OA (HOA) and cooking OA (COA), its relatively higher oxygen content suggests that emitted OA had undergone partial atmospheric oxidation. The OPOA spectrum was dominated by the $C_xH_y^+$ family (45%), while the $C_xH_yO^+$ and $C_xH_yO_z^+$ families together account for approximately 40% of the spectrum (Fig. S11). Key peaks appear at *m/z* 27, 28, 29, 41, 43, 44, 53, 55, 67, 69, 81, 83 and 91. Its average concentration was 0.09 μg m^{-3} and its O:C was consistent with similar OPOA factors reported in Beijing by Xu et al. (2019). OPOA showed a moderate correlation with particulate $PM_{0.1}$ NO_3 (R^2 = 0.41) (Fig. S13).

The absence of fresher factors in the PMF solution suggested the use of an external POA spectrum. For this study, a HOA factor derived from a wintertime field campaign previously conducted in Patras (Florou et al., 2017) was selected, ensuring compatibility with the study's conditions. The α-value approach was employed, testing a range of α-values from 0 to 0.3 in increments of 0.05 to assess the sensitivity of the results to rotational constraints.

A three-factor solution was selected in the ME-2 analysis as it provided the most effective representation of the OA sources. This solution identified two SOA factors (MO-OOA and LO-OOA) along with the constrained HOA factor (Fig. 9). The mass spectra for these factors are presented in Fig. S14.

Over the three-day observation period, the LO-OOA factor contributed approximately 70% of the total OA, with an average concentration of 0.4 μg m^{-3} and an O:C of 0.77. LO-OOA correlated quite well with particulate $PM_{0.1}$ sulfate (R^2 =0.64) and nitrate (R^2 =0.50). Its spectrum was dominated by oxygenated chemical families, which accounted for nearly 55% of the identified fragments. The MO-OOA factor, representing the most chemically aged component, accounted for 19% of the total OA with a mean concentration of 0.1 μg m^{-3}. It exhibited an O:C ratio of 0.84, with prominent spectral peaks at *m/z* 28 and 44, characteristic of highly oxidized organic compounds. Its correlation to $PM_{0.1}$ sulfate and nitrate was low to medium (R^2 = 0.26 and 0.47, respectively). The HOA factor was responsible for 11% of the measured OA with a mean concentration of 0.06 μg m^{-3}. There was no correlation with $PM_{0.1}$ sulfate (R^2 less than 0.1), while

https://doi.org/10.5194/egusphere-2025-1147
Preprint. Discussion started: 24 March 2025

weak correlations were observed with nitrate (R^2=0.26) and chloride (R^2=0.23). HOA had an O:C of 0.23, which is slightly higher than the typical values reported for freshly emitted HOA factors from HR-ToF-AMS spectra in urban environments (≤0.1). This elevated oxygenation level is likely attributable to the suburban location of the site, which is situated away from direct urban emissions and thus subject to less fresh (and less oxidized) aerosol inputs. Notably, previous studies have documented ambient HOA O:C within a similar range of 0.19–0.24 in suburban areas (Kostenidou et al., 2015; Gilardoni et al., 2014; Wu et al., 2022). The HOA spectrum was characterized by a high (57%) contribution of the $C_xH_y^+$ family (Fig. S14), and had prominent peaks at *m/z* 27, 29, 41, 43, 53, 55, 57, 67, 69, 71, 77, 79, 81, 83, and 91, all in accordance with previous studies regarding HOA.

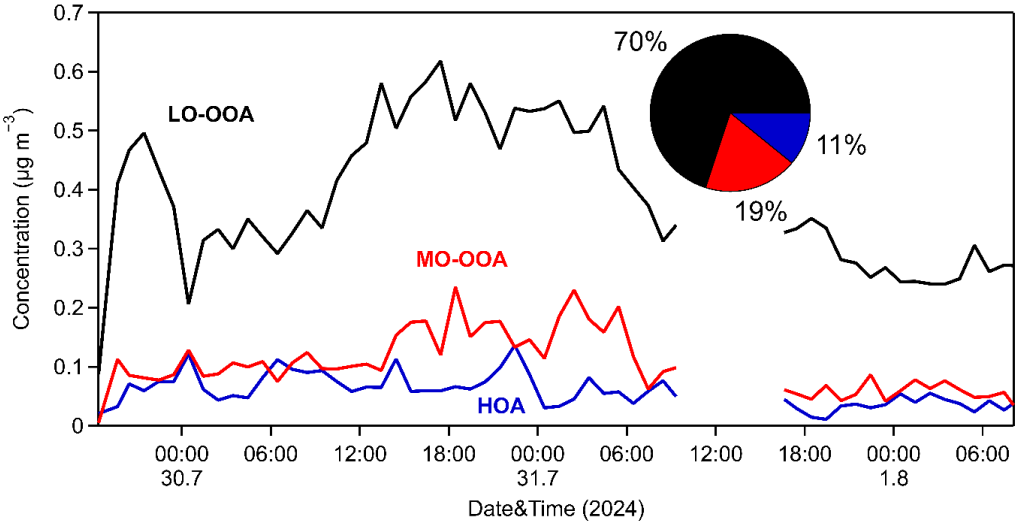

Figure 9. Hourly time-series of the ME-2 factors for $PM_{0.1}$ OA.

Upon comparing the solutions from the unconstrained PMF and ME-2 analyses, we observe that the OPOA and HOA factors exhibit similar time-series behavior (Fig. S15), with peaks occurring simultaneously. However, the OPOA factor shows more pronounced and higher peaks. Both factors contribute similarly to $PM_{0.1}$ OA, accounting for 16% and 11%, respectively. The primary difference between the ME-2 and PMF solutions lies in the contributions and spectra of the MO-OOA and LO-OOA factors. In the ME-2 analysis, the MO-OOA factor contributes

https://doi.org/10.5194/egusphere-2025-1147
Preprint. Discussion started: 24 March 2025

significantly less (19% compared to 45% in the PMF analysis), while the LO-OOA factor contributes substantially more (70% versus 39% in the PMF analysis) and displays a higher O:C ratio than the LO-OOA factor in the PMF solution.

Figure S16 illustrates the ratio of *m/z* 43 to the total OA (f_{43}) against the ratio of *m/z* 44 to the total OA (f_{44}) over the measurement period. These measurements are compared with the factor solutions derived from both the PMF and ME-2 analyses. This analysis indicated that fresh HOA had a surprisingly low contribution to $PM_{0.1}$ OA, if any. This is an interesting result that should be investigated in future studies.

7. Conclusions

This study introduces a new method for the continuous chemical characterization of $PM_{0.1}$, using an HR-ToF-AMS and an AAC operating as a $PM_{0.1}$-separator, followed by instruments that measure BC and elements. The development and evaluation of this system were conducted in a suburban area in Greece. These initial suburban measurements offer novel insights into the chemical characteristics, effective density and organic aerosol sources of ultrafine PM.

OA was the most abundant component of $PM_{0.1}$. Sulfates and calcium were the next most significant contributors, accounting for 14% and 18% of the total ultrafine mass, respectively. Ammonium contributed 7%, refractory black carbon (rBC) accounted for 4% and the sum of detected elements (Fe, K, Zn, Ti) for 7% of the total $PM_{0.1}$. Nitrate and chloride contributed less than 4% each, at 3% and 2%, respectively. Source apportionment suggested the presence of three sources of $PM_{0.1}$ OA. The majority of organic $PM_{0.1}$ was oxygenated OA, with contributions from both more oxidized and less oxidized fractions, together comprising 80–90% of $PM_{0.1}$ OA. Primary OA accounted for the remaining 10–15%.

The proposed approach has the potential to serve as a robust research system for detailed chemical characterization of $PM_{0.1}$, especially in urban locations where there are typically higher $PM_{0.1}$ concentrations, and many more nearby sources. This detailed $PM_{0.1}$ chemical characterization approach can contribute towards deeper investigations and better understanding of the potential link between ultrafine particle mass and human health.

Data availability. The data from this work are available upon request from Spyros Pandis (spyros@chemeng.upatras.gr).

https://doi.org/10.5194/egusphere-2025-1147
Preprint. Discussion started: 24 March 2025

Author contribution. G.A. developed the chemical characterization system and performed the field measurements. G.A. and K.F. performed the corresponding data analysis and wrote the paper. S.N.P. directed the study and edited the paper.

Competing interests. The authors report there are no competing interests to declare.

Financial support. This work was funded by the project NANOSOMs Grant 11504 of the Greek HFRI.

ORCID. Georgia Argyropoulou https://orcid.org/0009-0009-9993-931X, Kalliopi Florou https://orcid.org/0000-0001-9766-656X, Spyros Pandis https://orcid.org/0000-0001-8085-9795.

References

Abdillah, S. F., and Wang, Y. 2023. Ambient ultrafine particle ($PM_{0.1}$): Sources, characteristics, measurements and exposure implications on human health. *Environmental Research,* 218, 115061. https://doi.org/10.1016/j.envres.2022.115061

Argyropoulou, G. A., Kaltsonoudis, C., Patoulias, D., and Pandis, S. N. 2024. Novel method for the continuous mass concentration measurement of ultrafine particles ($PM_{0.1}$) with a water-based condensation particle counter (CPC). *Aerosol Science and Technology*, *58*, 1182-1193. https://doi.org/10.1080/02786826.2024.2368196

Baldauf, R.W., Devlin, R.B., Gehr, P., Giannelli, R., Hassett-Sipple, B., Jung, H., Martini, G., McDonald, J., Sacks, J.D., and Walker, K. 2016. Ultrafine Particle Metrics and Research Considerations: Review of the 2015 UFP Workshop. *International Journal of Environmental Research and Public Health*, 13, 1054. https://doi.org/10.3390/ijerph13111054

Beauchemin, S., Levesque, C., Wiseman, C. L., and Rasmussen, P. E. 2021. Quantification and characterization of metals in ultrafine road dust particles. *Atmosphere*, 12, 1564. https://doi.org/10.3390/atmos12121564

Cassee, F., Morawska, L., Peters, A., Wierzbicka, A., Buonanno, G., Cyrys, J., SchnelleKreis, J., Kowalski, M., Riediker, M., Birmili, W. and Querol, X., et al. 2019. White Paper: Ambient ultrafine particles: evidence for policy makers. https://efca.net/files/WHITE%20PAPER-UFP%20evidence%20for% 20policy% 20makers%20(25%20OCT).pdf

Canagaratna, M. R., Jimenez, J. L., Kroll, J. H., Chen, Q., Kessler, S. H., Massoli, P., Hildebrandt Ruiz, L., Fortner, E., Williams, L. R., Wilson, K. R., Surratt, J. D., Donahue, N. M., Jayne, J. T., and Worsnop, D. R. 2015. Elemental ratio measurements of organic compounds using aerosol mass spectrometry: Characterization, improved calibration, and implications. *Atmospheric Chemistry and Physics*, *15*, 253-272. https://doi.org/10.5194/acp-15-253-2015

Canonaco, F., Crippa, M., Slowik, J. G., Baltensperger, U., and Prévôt, A. S. 2013. SoFi, an IGOR-based interface for the efficient use of the generalized multilinear engine (ME-2) for the source apportionment: ME-2 application to aerosol mass spectrometer

https://doi.org/10.5194/egusphere-2025-1147
Preprint. Discussion started: 24 March 2025

data. *Atmospheric Measurement Techniques*, *6*, 3649-3661. https://doi.org/10.5194/amt-6-3649-2013

Corsini, E., Vecchi, R., Marabini, L., Fermo, P., Becagli, S., Bernardoni, V., Caruso, D., Corbella, L., Dell'Acqua, M., Galli, C. L., Lonati, G., Ozgen, S., Papale, A., Signorini, S., Tardivo, R., Valli, G., and Marinovich, M. 2017. The chemical composition of ultrafine particles and associated biological effects at an Alpine town impacted by wood burning. *Science of The Total Environment*, 587-588, 223-231. https://doi.org/10.1016/j.scitotenv.2017.02.125

Currie, L. A. 1995. Nomenclature in evaluation of analytical methods including detection and quantification capabilities (IUPAC recommendations 1995). *Pure and Applied Chemistry*, *67*, 1699-1723. https://doi.org/10.1351/pac199567101699

DeCarlo, P., Slowik, J., Worsnop, D., Davidovits, P., Jimenez, J. 2004. Particle morphology and density characterization by combined mobility and aerodynamic diameter measurements. Part 1: Theory. *Aerosol Science and Technology,* 38, 1185-1205. https://doi.org/10.1080/02786826.2004. 10399461.

DeCarlo, P. F., Kimmel, J. R., Trimborn, A., Northway, M. J., Jayne, J. T., Aiken, A. C., Gonin, M., Fuhrer, K., Horvath, T., Docherty, K. S., Worsnop, D. R., and Jimenez, J. L. 2006. Field-deployable, high-resolution, time-of-Flight aerosol mass spectrometer. *Analytical Chemistry*, *78*, 8281-8289. https://doi.org/10.1021/ac061249n

De Jesus, A. L., Rahman, M. M., Mazaheri, M., Thompson, H., Knibbs, L. D., Jeong, C., Evans, G., Nei, W., Ding, A., Qiao, L., Li, L., Portin, H., Niemi, J. V., Timonen, H., Luoma, K., Petäjä, T., Kulmala, M., Kowalski, M., Peters, A., Morawska, L. 2019. Ultrafine particles and $PM_{2.5}$ in the air of cities around the world: Are they representative of each other? *Environment International*, 129, 118-135. https://doi.org/10.1016/j.envint.2019.05.021

Donaldson, K., Stone, V., Clouter, A., Renwick, L., and MacNee, W. 2001. Ultrafine particles. *Occupational and Environmental Medicine*, 58, 211-216.

Eeftens, M., Phuleria, H. C., Meier, R., Aguilera, I., Corradi, E., Davey, M., Ducret-Stich, R., Fierz, M., Gehrig, R., Ineichen, A., Keidel, D., Probst-Hensch, N., Ragettli, M. S., Schindler, C., Künzli, N., and Tsai, M. 2015. Spatial and temporal variability of ultrafine particles, NO_2, $PM_{2.5}$, $PM_{2.5}$ absorbance, PM_{10} and PM_{coarse} in Swiss study areas. *Atmospheric Environment*, 111, 60-70. https://doi.org/10.1016/j.atmosenv.2015.03.031

Florou, K., Papanastasiou, D. K., Pikridas, M., Kaltsonoudis, C., Louvaris, E., Gkatzelis, G. I., Patoulias, D., Mihalopoulos, N., and Pandis, S. N. 2017. The contribution of wood burning and other pollution sources to wintertime organic aerosol levels in two Greek cities. *Atmospheric Chemistry and Physics*, *17*, 3145-3163. https://doi.org/10.5194/acp-17-3145-2017

Furger, M., Minguillón, M. C., Yadav, V., Slowik, J. G., Hüglin, C., Fröhlich, R., Petterson, K., Baltensperger, U., and Prévôt, A. S. 2017. Elemental composition of ambient aerosols measured with high temporal resolution using an online XRF spectrometer. *Atmospheric Measurement Techniques*, *10*, 2061-2076. https://doi.org/10.5194/amt-10-2061-2017

https://doi.org/10.5194/egusphere-2025-1147
Preprint. Discussion started: 24 March 2025

639 Giechaskiel, B., Melas, A., Martini, G., and Dilara, P. 2021. Overview of vehicle exhaust particle
640 number regulations. *Processes*, 9, 2216. https://doi.org/10.3390/pr9122216
641 Giechaskiel, B., Melas, A., Martini, G., Dilara, P., and Ntziachristos, L. 2022. Revisiting total
642 particle number measurements for vehicle exhaust regulations. *Atmosphere*, 13, 155.
643 https://doi.org/10.3390/atmos13020155
644 Gilardoni, S., Massoli, P., Giulianelli, L., Rinaldi, M., Paglione, M., Pollini, F., Lanconelli, C.,
645 Poluzzi, V., Carbone, S., Hillamo, R., Russell, L. M., Facchini, M. C., and Fuzzi, S. 2014.
646 Fog scavenging of organic and inorganic aerosol in the Po valley. *Atmospheric Chemistry*
647 *and Physics*, *14*, 6967-6981. https://doi.org/10.5194/acp-14-6967-2014
648 Halek, F., Kianpour-Rad, M., and Kavousirahim, A. 2010. Seasonal variation in ambient PM mass
649 and number concentrations (case study: Tehran, Iran). *Environmental Monitoring and*
650 *Assessment*, 169, 501-507.
651 HEI Review Panel on Ultrafine Particles. 2013. Understanding the Health Effects of Ambient
652 Ultrafine Particles. HEI Perspectives 3. Health Effects Institute, Boston, MA.
653 Hinds, W. C. 1999. *Aerosol technology: Properties, behavior, and measurement of airborne*
654 *particles*. John Wiley and Sons.
655 Jalava, P. I., Salonen, R. O., Pennanen, A. S., Sillanpää, M., Hälinen, A. I., Happo, M. S., Hillamo,
656 R., Brunekreef, B., Katsouyanni, K., Sunyer, J., and Hirvonen, M. 2007. Heterogeneities
657 in inflammatory and cytotoxic responses of RAW 264.7 macrophage cell line to urban air
658 coarse, fine, and ultrafine particles from six European sampling campaigns. *Inhalation*
659 *Toxicology*, 19, 213-225. https://doi.org/10.1080/08958370601067863
660 JRC Publications Repository. *Analytical measurement: Measurement uncertainty and*
661 *statistics.* https://publications.jrc.ec.europa.eu/repository/handle/JRC68476
662 Kim, J., Mulholland, G., Kukuck, S., and Pui, D. 2005) Slip correction measurements of certified
663 PSL nanoparticles using a nanometer differential mobility analyzer (nano-DMA) for
664 Knudsen number from 0.5 to 83. *Journal of Research of the National Institute of Standards*
665 *and Technology*, *110*, 31. https://doi.org/10.6028/jres.110.005
666 Kittelson, D., Khalek, I., McDonald, J., Stevens, J., and Giannelli, R. 2022. Particle emissions
667 from mobile sources: Discussion of ultrafine particle emissions and definition. *Journal of*
668 *Aerosol Science*, 159, 105881. https://doi.org/10.1016/j.jaerosci.2021.105881
669 Kostenidou, E., Pathak, R. K., and Pandis, S. N. 2007. An algorithm for the calculation of
670 secondary organic aerosol density combining AMS and SMPS data. *Aerosol Science and*
671 *Technology*, *41*, 1002-1010. https://doi.org/10.1080/02786820701666270
672 Kostenidou, E., Florou, K., Kaltsonoudis, C., Tsiflikiotou, M., Vratolis, S., Eleftheriadis, K., and
673 Pandis, S. N. 2015. Sources and chemical characterization of organic aerosol during the
674 summer in the Eastern Mediterranean. *Atmospheric Chemistry and Physics*, *15*, 11355-
675 11371. https://doi.org/10.5194/acp-15-11355-2015
676 Kumar, P., Wiedensohler, A., Birmili, W., Quincey, P., and Hallquist, M. 2016. *Ultrafine particles*
677 *pollution and measurements. The Quality of Air*, 73, 369-390. https://doi.org/10.1016/
678 bs.coac. 2016.04.004

https://doi.org/10.5194/egusphere-2025-1147
Preprint. Discussion started: 24 March 2025

Kuwayama Toshihiro, Chris R. Ruehl, and Michael J. Kleeman. 2013. Daily trends and source apportionment of ultrafine particulate mass ($PM_{0.1}$) over an annual cycle in a typical California city. *Environmental Science and Technology*, doi.org/10.1021/es403235c.

Kwon, H. S., Ryu, M. H., and Carlsten, C. 2020. Ultrafine particles: unique physicochemical properties relevant to health and disease. *Experimental and Molecular Medicine*, 52, 318-328, https://doi.org/10.1038/s12276-020-0405-1

Lanz, V. A., Alfarra, M. R., Baltensperger, U., Buchmann, B., Hueglin, C., and Prévôt, A. S. 2007. Source apportionment of submicron organic aerosols at an urban site by factor analytical modelling of aerosol mass spectra. *Atmospheric Chemistry and Physics*, *7*, 1503-1522. https://doi.org/10.5194/acp-7-1503-2007

Li, N., Sioutas, C., Cho, A., Schmitz, D., Misra, C., Sempf, J., Wang, M., Oberley, T., Froines, J., and Nel, A. 2003. Ultrafine particulate pollutants induce oxidative stress and mitochondrial damage. *Environmental Health Perspectives*, 111, 455-460. https://doi.org/10.1289/ehp.6000

Marcias, G., Fostinelli, J., Catalani, S., Uras, M., Sanna, A., Avataneo, G., De Palma, G., Fabbri, D., Paganelli, M., Lecca, L., Buonanno, G., and Campagna, M. 2018. Composition of metallic elements and size distribution of fine and Ultrafine particles in a Steelmaking factory. *International Journal of Environmental Research and Public Health*, 15, 1192. https://doi.org/10.3390/ijerph15061192

Marval, J., and Tronville, P. 2022. Ultrafine particles: A review about their health effects, presence, generation, and measurement in indoor environments. *Building and Environment*, 216, 108992. https://doi.org/10.1016/j.buildenv.2022.108992

Mataras, K., Siouti, E., Patoulias, D., and Pandis, S. 2024. Significant spatial and temporal variation of the concentrations and chemical composition of ultrafine particulate matter over Europe. EGUsphere [preprint]. https://doi.org/10.5194/egusphere-2024-3357

Moreno-Ríos, A. L., Tejeda-Benítez, L. P., and Bustillo-Lecompte, C. F. 2022. Sources, characteristics, toxicity, and control of ultrafine particles: An overview. *Geoscience Frontiers*, 13, 101147. https://doi.org/10.1016/j.gsf.2021.101147

Nel, A., Xia, T., Mädler, L., and Li, N. 2006. Toxic potential of materials at the Nanolevel. *Science*, 311, 622-627. https://doi.org/10.1126/science.1114397

Ohlwein S, Kappeler R, Kutlar Joss M, Künzli N, Hoffmann B. 2019. Health effects of ultrafine particles: a systematic literature review update of epidemiological evidence. *International Journal of Public Health*, 64, 547-559, https://doi.org/10.1007/s00038-019-01202-7.

Ostro, B., Hu, J., Goldberg, D., Reynolds, P., Hertz, A., Bernstein, L. and Kleeman, M. J. 2015. Associations of mortality with long-term exposures to fine and ultrafine particles, species and sources: results from the California Teachers Study Cohort. *Environmental Health Perspectives*, 123, 549-556, https://doi.org/10.1289/ehp.1408565.

Paatero, P., and Tapper, U. 1994. Positive matrix factorization: A non-negative factor model with optimal utilization of error estimates of data values. *Environmetrics*, *5*, 111-126. https://doi.org/10.1002/env.3170050203

https://doi.org/10.5194/egusphere-2025-1147
Preprint. Discussion started: 24 March 2025

Paatero, P. 1999. The multilinear engine: A table-driven, least squares program for solving multilinear problems, including the N-way parallel factor analysis model. *Journal of Computational and Graphical Statistics*, *8*, 854. https://doi.org/10.2307/1390831

Phairuang, W., Inerb, M., Hata, M., and Furuuchi, M. 2022. Characteristics of trace elements bound to ambient nanoparticles ($PM_{0.1}$) and a health risk assessment in southern Thailand. *Journal of Hazardous Materials*, 425, 127986. https://doi.org/10.1016/j.jhazmat.2021.127986

Schraufnagel, D. E. 2020. The health effects of ultrafine particles. *Experimental and Molecular Medicine*, 52, 311-317, https://doi.org/10.1038/s12276-020-0403-3.

Seinfeld, J. H., and Pandis, S. N. 2016. *Atmospheric Chemistry and Physics: From Air Pollution to Climate Change*, 3rd edition, Wiley and Sons, New York.

Tavakoli, F., and Olfert, J. S. 2013. An instrument for the classification of aerosols by particle relaxation time: Theoretical models of the aerodynamic aerosol classifier. *Aerosol Science and Technology*, *47*, 916-926. https://doi.org/10.1080/02786826.2013.802761

Tavakoli, F., and Olfert, J. S. 2014. Determination of particle mass, effective density, mass–mobility exponent, and dynamic shape factor using an aerodynamic aerosol classifier and a differential mobility analyzer in tandem. *Journal of Aerosol Science*, *75*, 35-42. https://doi.org/10.1016/j.jaerosci.2014.04.010

Taylor, J. W., Allan, J. D., Liu, D., Flynn, M., Weber, R., Zhang, X., Lefer, B. L., Grossberg, N., Flynn, J., and Coe, H. 2015. Assessment of the sensitivity of core / shell parameters derived using the single-particle soot photometer to density and refractive index. *Atmospheric Measurement Techniques*, *8*, 1701-1718. https://doi.org/10.5194/amt-8-1701-2015

Timko, M. T., Yu, Z., Kroll, J., Jayne, J. T., Worsnop, D. R., Miake-Lye, R. C., Onasch, T. B., Liscinsky, D., Kirchstetter, T. W., Destaillats, H., Holder, A. L., Smith, J. D., and Wilson, K. R. (2009). Sampling artifacts from conductive silicone tubing. *Aerosol Science and Technology*, *43*, 855-865. https://doi.org/10.1080/02786820902984811

Tremper, A. H., Font, A., Priestman, M., Hamad, S. H., Chung, T., Pribadi, A., Brown, R. J., Goddard, S. L., Grassineau, N., Petterson, K., Kelly, F. J., and Green, D. C. 2018. Field and laboratory evaluation of a high time resolution X-ray fluorescence instrument for determining the elemental composition of ambient aerosols. *Atmospheric Measurement Techniques*, *11*, 3541-3557. https://doi.org/10.5194/amt-11-3541-2018

Tronville, P., Gentile, V., and Marval, J. 2023. Guidelines for measuring and reporting particle removal efficiency in fibrous media. *Nature Communications*, 14. https://doi.org/10.1038/s41467-023-41154-4

Ulbrich, I. M., Canagaratna, M. R., Zhang, Q., Worsnop, D. R., and Jimenez, J. L. 2009. Interpretation of organic components from positive matrix factorization of aerosol mass spectrometric data. *Atmospheric Chemistry and Physics*, *9*, 2891-2918. https://doi.org/10.5194/acp-9-2891-2009

U.S. EPA. 2019. Integrated Science Assessment (ISA) for Particulate Matter (EPA Document No. EPA 600/R-19/188), U.S. Environmental Protection Agency.

https://doi.org/10.5194/egusphere-2025-1147
Preprint. Discussion started: 24 March 2025

759 Weichenthal, S., Bai, L., Hatzopoulou, M. et al. 2017. Long-term exposure to ambient ultrafine
760 particles and respiratory disease incidence in in Toronto, Canada: a cohort study.
761 *Environmental Health*, 16, 64. https://doi.org/10.1186/s12940-017-0276-7
762 Wu, Y., Liu, D., Tian, P., Sheng, J., Liu, Q., Li, R., Hu, K., Jiang, X., Li, S., Bi, K., Zhao, D.,
763 Huang, M., Ding, D., and Wang, J. 2022. Tracing the formation of secondary aerosols
764 influenced by solar radiation and relative humidity in suburban environment. *Journal of*
765 *Geophysical Research: Atmospheres*, *127*. https://doi.org/10.1029/2022jd036913
766 Xu, W., Sun, Y., Wang, Q., Zhao, J., Wang, J., Ge, X., Xie, C., Zhou, W., Du, W., Li, J., Fu, P.,
767 Wang, Z., Worsnop, D. R., and Coe, H. 2019. Changes in aerosol chemistry from 2014 to
768 2016 in winter in Beijing: Insights from high-resolution aerosol mass
769 spectrometry. *Journal of Geophysical Research: Atmospheres*, *124*, 1132-
770 1147. https://doi.org/10.1029/2018jd029245
771 Xue, W., Xue, J., Mousavi, A., Sioutas, C., and Kleeman, M. J. 2020a. Positive matrix factorization
772 of ultrafine particle mass ($PM_{0.1}$) at three sites in California. *Science of The Total*
773 *Environment*, 715, https://doi.org/10.1016/j.scitotenv.2020.136902.
774 Xue, W., Xue, J., Shirmohammadi, F., Sioutas, C., Lolinco, A., Hasson, A., and Kleeman, M. J.
775 2020b. Day-of-week patterns for ultrafine particulate matter components at four sites in
776 California. *Atmospheric Environment*, 222, https://doi.org/10.1016/j.atmosenv.
777 2019.117088.
778 Yu, X., Venecek, M., Kumar, A., Hu, J., Tanrikulu, S., Soon, S. T., Tran, C., Fairley, D. and
779 Kleeman, M. J. 2019. Regional sources of airborne ultrafine particle number and mass
780 concentrations in California. *Atmospheric Chemistry and Physics*, 19, 14677-14702,
781 https://doi.org/10.5194/acp-19-14677-2019.
782 Zhang, R., Wang, G., Guo, S., Zamora, M. L., Ying, Q., Lin, Y., Wang W., Hu M. and Wang, Y.
783 2015. Formation of urban fine particulate matter. *Chemical Reviews*, 115, 3803-3855,
784 https://doi.org/10.1021/acs.chemrev.5b00067